

Physics

Feasibility of an MRI-only workflow for postimplant dosimetry of low-dose-rate prostate brachytherapy: Transition from phantoms to patients

Reyhaneh Nosrati^{1,2,*}, William Y. Song³, Matthew Wronski^{4,5}, Ana Pejović-Milić¹, Gerard Morton^{5,6}, Greg J. Stanisz^{1,2,7}

¹Department of Physics, Ryerson University, Toronto, Canada

²Physical Sciences Platform, Sunnybrook Research Institute, Toronto, Canada

³Department of Radiation Oncology, Virginia Commonwealth University, Richmond, VA

⁴Department of Medical Physics, Sunnybrook Health Sciences Centre, Toronto, Canada

⁵Department of Radiation Oncology, University of Toronto, Toronto, Canada

⁶Department of Radiation Oncology, Odette Cancer Centre, Sunnybrook Health Sciences Centre, Toronto, Canada

⁷Department of Medical Biophysics, University of Toronto, Toronto, Canada

ABSTRACT

PURPOSE: The lack of positive contrast from brachytherapy seeds in conventional MR images remains a major challenge toward an MRI-only workflow for postimplant dosimetry of low-dose-rate brachytherapy. In this work, the feasibility of our recently proposed MRI-only workflow in clinically relevant scenarios is investigated and the necessary modifications in image acquisition and processing pipeline are proposed for transition to the clinic.

METHODS AND MATERIALS: Four prostate phantoms with a total of 321 I-125 implanted dummy seeds and three patients with a total of 168 implanted seeds were scanned using a gradient echo sequence on 1.5 T and 3T MR scanners. Quantitative susceptibility mapping (QSM) was performed for seed visualization. Before QSM, the seed-induced distortion correction was performed followed by edge enhancement. Seed localization was performed using spatial clustering algorithms and was compared with CT. In addition, feasibility of the proposed method on detection of prostatic calcifications was studied.

RESULTS: The proposed susceptibility-based algorithm generated consistent positive contrast for the seeds in phantoms and patients. All the 321 seeds in the four phantoms were correctly identified; the MR-derived seeds centroids agreed well with CT-derived positions (average error = 0.5 ± 0.3 mm). The proposed algorithm for seed visualization was found to be orientation invariant. In patient cases, all seeds were visualized and correctly localized (average error = 1.2 ± 0.9 mm); no significant differences between dose volume histogram parameters were found. Prostatic calcifications were depicted with negative contrast on QSM and spatially agreed with CT.

CONCLUSIONS: The proposed MRI-based approach has great potential to replace the current CT-based practices. Additional patient studies are necessary to further optimize and validate the workflow. © 2019 American Brachytherapy Society. Published by Elsevier Inc. All rights reserved.

Keywords:

MRI-only workflow; Quantitative susceptibility mapping (QSM); Brachytherapy seeds; Unsupervised machine learning; Postimplant dosimetry

Received 21 March 2019; received in revised form 12 June 2019; accepted 20 June 2019.

Conflict of Interest: The authors report no conflicts of interest in any product mentioned or concept discussed in this article.

* Corresponding author. Sunnybrook Research Institute, S605, 2075 Bayview Avenue, Toronto, Ontario M4N 3M5, Canada. Tel.: +1 416 732 0994; fax: +1 416-480-5714.

E-mail address: Reyhaneh.Nosrati@childrens.harvard.edu (R. Nosrati).

Introduction

Permanent implantation of low-dose-rate (LDR) brachytherapy seeds is a well-established treatment modality for patients with localized prostate cancer. The American Brachytherapy Society and the Groupe Européen de Curiothérapie—European Society for Therapeutic Radiology and Oncology recommends evaluating the quality

of the implant and the dose distribution within 60 days of implantation using standard computed tomography (CT) (1,2). Seeds have excellent positive contrast on CT images; however, owing to the relatively poor soft tissue contrast in CT, anatomical delineation is very challenging and significant interobserver and intraobserver variabilities have been reported in the CT-based approach (3–5).

It is widely accepted that magnetic resonance imaging (MRI) is a better imaging modality for delineation of the prostate and the nearby organs at risk; however, owing to the lack of MR signal from the seeds, they appear as dark voids on conventional MR images which are indistinguishable from other such voids associated with calcifications, air cavities, and blood vessels. Thus, CT and MRI are complementary modalities to provide both clear seed identification as well as high contrast anatomical visualization of the prostate. Clinical workflows using CT-MRI registration taking advantage of both imaging modalities is currently implemented at many centers; however, this involves additional resources, patient transfers and image registration error (6–8). An MRI-only workflow for postimplant dosimetry of LDR brachytherapy seeds thus would be an ideal solution for many clinics.

Although several MRI-only approaches have been proposed for seed depiction and localization, none of them have demonstrated robust performance translatable to the clinic. Zijlstra *et al.* have investigated the feasibility of an MRI-based workflow in which the seed-induced magnetic field distortions were simulated at different orientations and were used for template matching in realistic cases; although the proposed method has acceptable performance in detection of spaced seeds (average error of 0.8 ± 0.4 mm), by average 33% of the clumped seeds were not identified because of complexity of the field distortion around those seeds (9). In addition, the radiation oncologists prefer to clearly observe the seeds for verification of the postplanning seed finder algorithm but the proposed method is not able to portray the seeds with positive contrast. Other studies have proposed new pulse sequences such as IRON and co-RASOR that utilize susceptibility-induced signal pileup around seeds to generate positive contrast; however, these methods require nonclinical pulse sequences and the reconstructed positive contrast seed is either diffused around the seed position or strongly depends on seed orientation (10–12). Susceptibility-based positive contrast and quantitative susceptibility mapping (QSM) for seeds visualization has also been studied but the proposed methods rely on nonclinical MR pulse sequences or scanners; moreover, the quality of the reconstructed seed images using these methods is significantly worse than that on CT and seed visualization is orientation-dependent (13–15). A novel MR marker (C4) has also been proposed as a spacer between seeds on a strand which is visible on MR images. Although C4 markers appear with positive contrast on MR images, there are several limitations associated with their application which include limited availability and

higher cost compared with standard stranded seeds, necessity of endorectal coil for optimal marker visualization, limited usage for clumped and nonstranded seed applications, and seed localization error due to lack of positive contrast from the seeds rather than spacer (16–19).

Recently Nosrati *et al.* (20) have proposed an MRI-only pipeline based on QSM and unsupervised machine learning (ML) for seed visualization and localization in a simple agar phantom with small number of seeds. In that study, data clustering, which is the most well-known unsupervised ML algorithm, was used for spatial localization of the seeds. Unlike supervised ML, unsupervised learning does not require labeled training data and the algorithm learns to partition the data into several clusters based on their similarities. The method proposed in the study by Nosrati *et al.* (20) showed high efficiency in a simple agar phantom; however, a number of limitations needed to be addressed including realistic seed configurations, seed orientation dependence of the algorithm, absence of clumped seeds, correction of the seed-induced MR image distortions, absence of any patient-related physiological noise, unrealistic uniformity of the imaging volume, and absence of organs at risk for dosimetric analysis.

Materials and methods

Phantoms

Four realistic prostate phantoms (CIRS Inc. 053L model) which contained a simulated prostate gland with three lesions as well as a simulated urethra and rectum were used. Phantoms were imaged using transrectal ultrasound and the preplans (needle loading plans) were generated accordingly in the VariSeed software (Varian, Palo Alto, CA). The phantoms were implanted under transrectal ultrasound image guidance comprising a total of 321 I-125 dummy stranded seeds (IsoAid Advantage USA). The needle loading plans included a total of six double and one triple-loaded seeds.

Patients

Three patients participated in this study; two patients received standard whole gland brachytherapy with 78 and 66 implanted stranded seeds (I-125, IsoAid Advantage). The third patient was a participant in a phase I/II clinical trial of focal brachytherapy with 24 stranded seeds (I-125, IsoAid Advantage) implanted in the MR-defined dominant intraprostatic lesion. There were a total of eight double loading (16 clumped seeds in total) in the patients' LDR treatment plan. Both patients who underwent whole-gland LDR brachytherapy had prostatic calcifications confirmed with CT. Currently, at the center where this study was conducted, the standard of care for postimplant dosimetry of prostate LDR brachytherapy requires both CT and MR scan within 1 month after seed implantation procedure. In

addition to the standard of care, which included the turbo spin-echo T1-, T2- and diffusion-weighted MRI, for MRI-based seed identification, these patients underwent a gradient echo sequence during the same MR scan.

Data acquisition parameters

The phantoms were scanned with a 3D multi echo gradient recalled echo sequence at both 1.5 T MRI (Philips Ingenia) and 3T MRI (Philips Achieva) scanners using an 8-channel head coil array. The pulse sequence parameters on 3T scanners were $TE_1/TR = 2.3/15.7$ ms; number of echoes = 3; flip angle = 15° ; FOV = $140 \times 140 \times 100$ mm³; resolution = $0.8 \times 0.8 \times 1$ mm³. The pulse sequence parameters on 1.5 T scanners were $TE_1/TR = 2.2/10.3$ ms; number of echoes = 4; flip angle = 20° ; FOV = $140 \times 140 \times 100$ mm³; resolution = $0.8 \times 0.8 \times 1$ mm³. The acquisition time was approximately 8 min. To evaluate the performance of the proposed method for different orientations of the seeds with respect to the static magnetic field (B_0), the phantoms were scanned at three different angles with respect to the B_0 : 0° , 45° , and 90° .

The patients were scanned with a 3T MRI scanner (Philips Achieva) with a 16-channel torso coil (Sense XL Torso). A 3D multi echo gradient recalled echo sequence with fat suppression using ‘‘Spectral Presaturation with Inversion Recovery’’ method and in-phase echo times (for field map estimation and to minimize the chemical shift artifact due to water fat phase cancellation) with the following parameters was utilized: $TE_1/TR = 2.3/15.7$ ms; number of echoes = 3; flip angle = 15° ; FOV = $224 \times 224 \times 120$ mm³; resolution = $1 \times 1 \times 1.5$ mm³. To minimize the motion (breathing) artifact, the anterior-posterior direction was chosen as the frequency encoding direction (9). The scan time for the patient was approximately 10 min. Owing to scan time constraints in patients, the slice thickness was increased to 1.5 mm; this should not affect the seed identification accuracy because most of the seed are oriented almost parallel to the axial direction, and the 1.5 mm axial slice thickness is three times smaller than the length of the seed in that direction (4.5 mm).

The CT scanning parameters were set to a standard clinical protocol used for routine postimplant dosimetry evaluations: 120 kVp, 400 mAs, and 3 mm slice thickness which was reconstructed at 1.5 mm thickness.

Geometrical distortion correction

The seed-induced geometrical distortions in MR images were corrected using the magnitude and phase images acquired by the GRE sequence. In general, all MRI pulse sequences generate two kinds of images: magnitude and phase. Magnitude images have the maximum signal-to-noise ratio and are used for most diagnostic purposes in the clinic; phase images are used occasionally in specific

applications such as flow measurement and field mapping. To estimate and correct the image distortions, the field map was estimated using phase images then magnitude images were corrected accordingly. The field map estimation and image correction were performed in k-space domain. The k-space data, $y(t)$ and the system matrix, $A(\omega, t)$ were calculated using the MIRT toolbox (21). The method of Matakos *et al.* for joint estimation of undistorted field map (ω) and corrected images (q) was used for distortion correction; the following optimization problem was iteratively solved via the preconditioned conjugate gradients algorithm (22–25):

$$\hat{\omega}, \hat{q} = \underset{q, \omega}{\operatorname{argmin}} \|y(t) - A(\omega, t)q^k\|_2^2 + \lambda_i \|Cq\|_2^2 + \lambda_f \|C\omega\|_2^2 \quad (1)$$

where C is a second-order difference operator and λ_i and λ_f are the image and field map estimation regularization parameters and were chosen such that the full-width-half-maximum of the point-spread-function was 1.1 pixels. An initialization for the field map was introduced as the difference between two consecutive distorted phase images normalized to the ΔTE .

Quantitative susceptibility mapping using MEDI+0

The diagram in Fig. 1 shows the proposed workflow for seed visualization and detection. Seed visualization was based on a modified QSM algorithm. In principal, the relative local field disturbance can be approximated as the convolution of the dipole kernel and the local magnetic susceptibility (26,27), therefore theoretically given the local field map, $b(r)$ and the dipole kernel, $d(r)$ the susceptibility, $\chi(r)$ can be calculated in the Fourier domain as following:

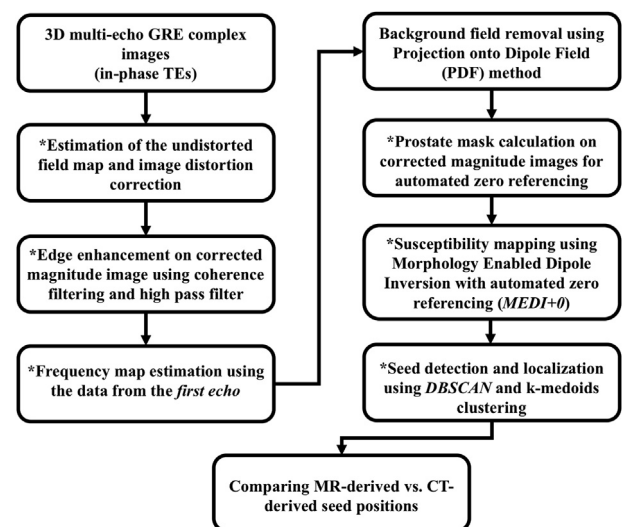


Fig. 1. The schematics of the proposed workflow for brachytherapy seed visualization and detection. The steps shown by the ‘‘*’’ indicate the proposed postprocessing modifications compared with the previously proposed method (20).

$$b(r) = d(r) \otimes \chi(r) \xrightarrow{\text{Fourier Transform}} B(k) = D(k) \times \chi(k) \Rightarrow \chi(k) = \frac{B(k)}{D(k)} \quad (2)$$

$$d(r) = \frac{3 \cos^2 \theta_r - 1}{4\pi r^3} \xrightarrow{\text{Fourier Transform}} D(K) = \frac{1}{3} - \frac{k_z^2}{k^2} \quad (3)$$

Dipole kernel, $d(r)$ is the magnetic field generated by a unit dipole at the origin which is zero at $\theta = 54.57$. Therefore, field to susceptibility inversion problem in Equation 2 is ill-posed requires regularization.

The 3D susceptibility map was calculated in the following steps: after distortion correction and edge enhancement, the frequency map (f_r) was estimated using the distortion-corrected magnitude (M) and phase (θ) images obtained at the first echo by solving the following exponential minimization problem:

$$f_{r,\theta_{or}} = \operatorname{argmin} \left\| M_{r,TE_1} e^{i\theta_{r,TE_1}} - M_{r,TE_1} e^{i(f_r \times TE_1 + \theta_{r,0})} \right\|_2^2 \quad (4)$$

The background field was calculated using projection onto dipole field method (28) and was subtracted from the frequency map. Finally, the susceptibility map was calculated using morphology-enabled dipole inversion with automated prostate zero referencing (MEDI+0). Morphology-enabled dipole inversion (MEDI) refers to the application of morphological (edge) information of the magnitude images in susceptibility calculation by matching the edges between magnitude image and the reconstructed susceptibility map. Prostate zero referencing reduces the susceptibility inhomogeneity within the background prostate tissue. The following regularization problem was solved iteratively using conjugate gradient method (29–31):

$$\chi_r = \operatorname{argmin}_{\chi_r} \left\| W [e^{iD_r \chi_r} - e^{if_r}] \right\|_2^2 + \lambda_1 \|G'_M G_\chi\|_1 + \lambda_2 \|M[\chi_r - \bar{\chi}_p]\|_2^2 \quad (5)$$

where D_r is the Fourier domain dipole kernel; f_r is the off-resonance frequency map (after background field removal); W is a weighting matrix calculated using a binary mask normalized to the noise standard deviation; W was tuned at each iteration using the Model Error Reduction Through Iterative Tuning technique (31); G is the gradient operator; M is a binary mask calculated by thresholding the undistorted magnitude images to roughly segment the prostate and muscles for zero referencing; $\bar{\chi}_p$ is the average estimated susceptibility within the segmented volume. The L1 regularization term minimizes the number of voxels corresponding to an edge in estimated susceptibility map but not an edge in the magnitude (29,32,33). The second L2 regularization term enforces susceptibility homogeneity within the prostate and reduces the artifacts around the seeds in the reconstructed QSM (30).

To achieve optimal seed reconstruction (in both shape and size) through QSM, before dipole inversion, the edges of the magnitude images were enhanced using the coherence filtering followed by a Fourier-based high-pass filter (34).

Seed localization and dosimetric comparison

The estimated susceptibility maps were thresholded at 20% of the maximum susceptibility value for each subject. Seed centroids were identified using unsupervised ML algorithms in MATLAB based on density-based spatial clustering of applications with noise (DBSCAN) followed by the K-medoid clustering for connected clusters (clumped seeds) (35–37). The disconnected (spaced) seeds were localized using DBSCAN algorithm. The average number of points in each cluster for an individual seed was calculated; then K-medoid clustering was performed on clusters which exceed the average number of points to localized clumped (nonspaced) seeds. Seed orientations were not taken into account for dosimetric analysis.

The seed localization on CT images was performed in MIM software (MIM Symphony Dx). To compare the MR-based seed positions with that of CT, the estimated seed centroids using the proposed MR-based workflow were registered to those calculated by the clinical CT-based software (MIM Symphony). Before registration, the MRI (QSM and T2-weighted) and CT images were registered on MIM Symphony and the agreement between the positive contrast seed positions on CT and MR (QSM) were visually (qualitatively) inspected. To register the MR- and CT-derived seed positions, first one representative seed centroids was chosen on QSM and the corresponding seeds was identified on CT (for instance the most superior/inferior seed) and a rough (initial) translation matrix (from MRI to CT) was calculated between the two points. The initial estimated translation was applied to all MR-based centroids and then an automated registration was performed for fine tuning the registration. The final rotation and translation matrix between the two point clouds was calculated using a rigid registration framework based on Iterative Closest Point algorithm (38).

To analyze the dosimetric effect of the estimated MR-based seed positions vs. the conventional CT-based approach, prostate, urethra (only in phantoms), and rectum were contoured on CT images and accumulative dose volume histograms (DVH curves) were calculated in MIM software first with CT-derived seed positions and subsequently using the MR-derived positions. The dose to 90% of the prostate volume (D_{90}), the prostate volume that receives 100%, 150%, and 200% of the prescribed dose (V_{100} , V_{150} , and V_{200}), and the dose to 2 cm³ of the rectum and urethra ($D_{2cc,rectum}$, $D_{2cc,urethra}$) were compared between the two methods.

Two-tailed paired sample t -test was used to evaluate the significance of the difference between CT- and MRI-

derived seed positions and dosimetric parameters. Statistical analysis was performed using the SPSS software (IBM SPSS statistics 24). Statistical significance was assumed to be at $p < 0.05$. To assess the agreement between the seed positions using the proposed algorithm vs. the standard CT-based method the Bland-Altman analysis with 95% confidence interval was performed.

Results

Phantom results

Seed visualization at different orientations with respect to B_0

One of the prostate phantoms with 70 implanted seeds and the associated raw magnitude and phase MR images are illustrated in Figs. 2a–2d. The maximum intensity projections reconstruction of the calculated susceptibility maps at three different angular positions as well as CT images are shown in Figs. 2e–2h. As shown in Figs. 2e–2g, the proposed seed visualization algorithm was not affected by the seed orientation and changing the orientation of the

phantoms (seeds) did not affect the seed reconstruction. In phantoms, the new proposed algorithm and the method proposed by Nosrati et al. (20) generated visually similar susceptibility maps. However, the distortion correction step reduced the seed localization error which is discussed in the following section.

MR-based seed localization and dosimetric analysis

All 321 implanted seeds in phantoms were correctly detected. Figures 3a–3d shows comparisons between seed positions estimated by the proposed MR-based algorithm and the clinical CT-based seed finder in all four phantoms. The maximum and average distance \pm standard deviation between the CT- and MR-derived positions for all 321 seeds were 1.3 mm and 0.5 ± 0.3 mm, respectively, whereas, without distortion correction and applying the K-means clustering as proposed in (20) one of the seeds in the triple-loaded strand was misdetected and the maximum and average errors (excluding the misdetected seed) were 2.9 mm and 0.9 ± 1.1 , respectively.

The differences in seed positions for each phantom approximated to a Gaussian distribution that was confirmed

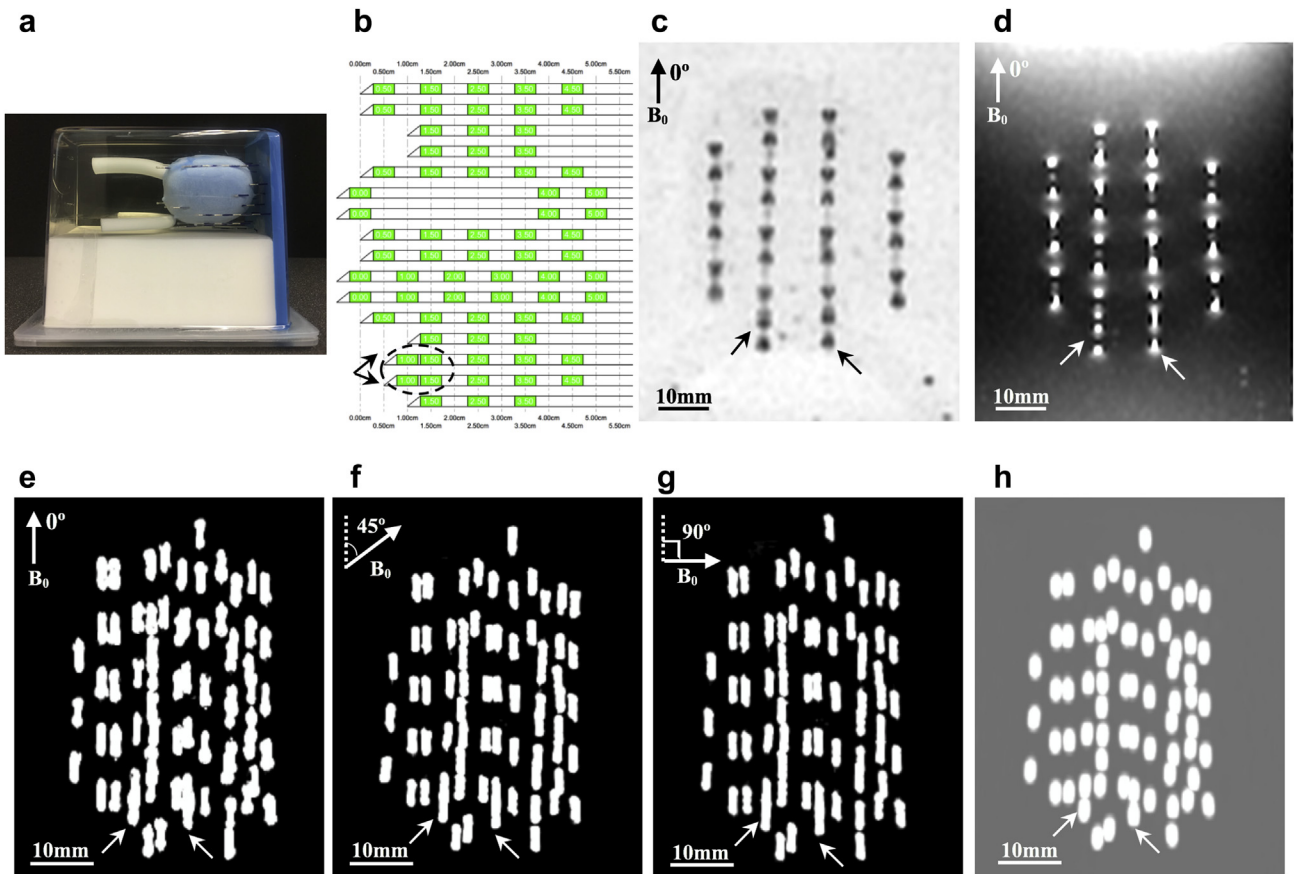


Fig. 2. (a) One sample phantom with 70 implanted seeds; (b) the seed implantation plan (needle loading) which contained four clumped seeds shown by the arrows; (c) the Minimum Intensity Projection (MinIP) of the magnitude image from 20 slices at the shortest TE; (d) the maximum intensity projection (MIP) of the phase image from 20 slices at the shortest TE. The full-thresholded MIP of the calculated susceptibility maps with the phantom orientated at (e) 0°, (f) 45°, and (g) 90° with respect to the static magnetic field (B_0); (h) the MIP of the CT image of the same phantom. The arrows in (b–g) indicate the clumped (double-loaded on a strand) seeds.

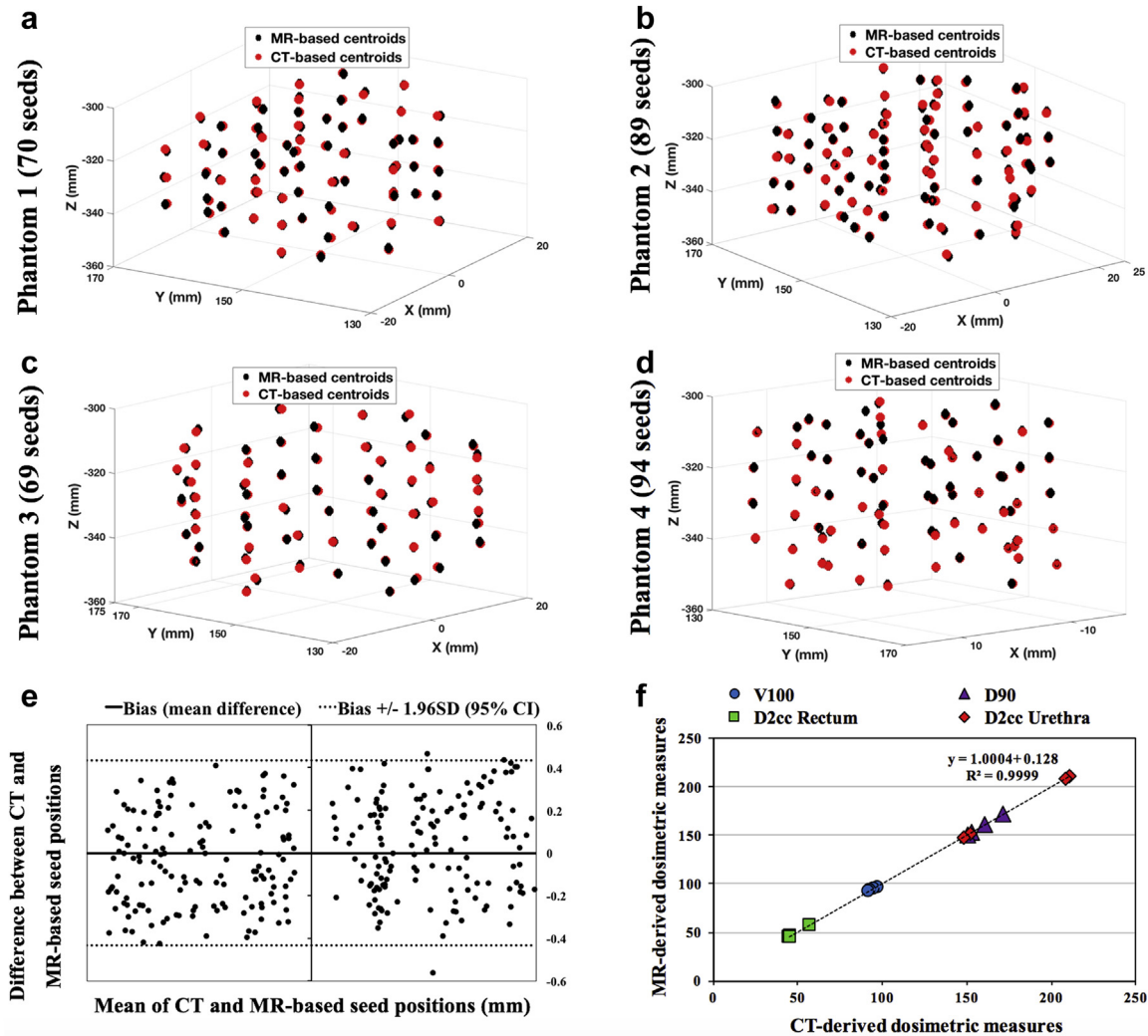


Fig. 3. (a–d) Comparison between clinical CT-based (MIM Symphony) and the proposed MR-based seed localizer algorithms on each of four phantoms; (e) the Bland-Altman plot for CT- and MR-derived seed positions for all 321 seeds; (f) the correlation between MR- and CT-derived DVH parameters. DVH = dose volume histogram.

by Kolmogorov-Smirnov normality test ($p > 0.3$). Bland-Altman analysis of MR-based compared with CT-derived seed centroids revealed a very small bias of -0.0005 mm with narrow $[-0.43 + 0.43]$ mm 95% limits of agreement; as shown in Fig. 3e, only two of 321 seeds were marginally out of the 95% confidence interval level.

The DVH parameters including prostate D_{90} , V_{100} , V_{150} , and V_{200} , as well as $D_{2cc,rectum}$ and $D_{2cc,urethra}$ are summarized in Table 1. The differences between CT/MR-derived DVH parameters were less than 1.5%. The correlation between MR- and CT-based DVH indices is illustrated in Fig. 3f showing excellent agreement between them ($R^2 > 0.99$).

Patient studies

MR-based seed visualization

Figures 4a–4d illustrates different steps of the proposed pre-QSM processing pipeline for the patient with 78

implanted seeds. The estimated distortion map which was calculated as the field map normalized to the bandwidth scaled by the voxel size is shown in Fig. 4a; the maximum distortion was 1.1 mm observed near the seeds. The difference between distorted and undistorted magnitude images is shown in Fig. 4c.

Figure 5 shows the CT image, corrected magnitude and phase images, prostate and muscle mask for zero referencing, and the MEDI, MEDI+0 with and without distortion correction results for one axial cross-section of the prostate.

The effectiveness of each of the proposed modifications in the QSM pipeline is demonstrated in Figs. 5e–5h. The efficiency of algorithm proposed in the study by Nosrati et al (20) was significantly degraded in patients compared with the phantoms, and seed reconstruction was unsuccessful particularly near the prostate boundaries (Fig. 5e). The key changes in acquisition and postprocessing pipeline were changes to the MR pulse sequence parameters,

Table 1

The summary of dosimetric parameters obtained from DVH curves calculated using CT- and MR-derived seed positions

	D_{90} (Gy)		V_{100} (%)		V_{150} (%)		V_{200} (%)		$D_{2cc, rectum}$ (Gy)		$D_{2cc, urethra}$ (Gy)	
	CT	MRI	CT	MRI	CT	MRI	CT	MRI	CT	MRI	CT	MRI
Phantom 1	172.1	171.6	97.3	97.2	70.5	70.3	26.0	26.2	46.2	46.3	211.5	211.7
% Difference	0.3%		0.1%		0.3%		0.7%		0.2%		0.1%	
Phantom 2	161.1	160.9	94.9	94.9	61.0	60.4	20.1	20.1	45.1	45.1	208.6	208.6
% Difference	0.1%		0%		1.0%		0.1%		0%		0%	
Phantom 3	153.6	153.9	93.3	93.4	44.6	44.3	17.5	17.5	45.5	45.7	152.3	151.7
% Difference	0.2%		0.1%		0.7%		0.5%		0.4%		0.4%	
Phantom 4	151.3	150.7	92.4	92.3	43.4	42.9	15.0	15.2	57.6	57.9	148.3	147.8
% Difference	0.4%		0.1%		1.0%		1.4%		0.5%		0.3%	
Patient 1	143.3	144.5	89.2	89.6	35.6	34.2	14.2	14.3	69.8	69.0	–	–
% Difference	0.8%		0.5%		1.9%		0.8%		1.1%		–	
Patient 2	158.3	160	93.7	93.2	57.2	56.9	23.3	23.3	92.2	92.2	–	–
% Difference	1.1%		0.6%		0.5%		0%		0%		–	

DVH = dose volume histogram.

seed-induced distortion correction, eliminating the phase unwrapping step, using only the first echo for frequency map estimation, edge enhancement and optimizing the edge threshold for extracting morphological information from magnitude image (required for MEDI), optimizing regularization parameters in patients, and finally applying prostate zero referencing (MEDI+0). The image postprocessing pipeline took approximately 6 min per patient to visualize and localize the seeds.

The MEDI+0 technique significantly improved the homogeneity of the prostate and muscles while unaffected the seeds. In addition, the artifacts around the reconstructed seeds in QSM were significantly reduced by applying the MEDI+0 algorithm. Distortion correction improved the spatial accuracy of the susceptibility mapping; the arrow in Fig. 5g and h indicates one seed which was better depicted after distortion correction.

Figure 6 shows the T2-weighted MR image, maximum intensity projection reconstruction of the CT, and the processed MR images (QSM) for all three patients. The quality of the seed visualization in processed MR images with the proposed method is comparable with that on CT. It should be noted that some observed visual differences between CT and QSM axial slices shown in Fig. 6 may be because of prostate deformation between two scans as well as the

differences in image acquisition parameters (slice thickness) between CT and MRI.

As shown in Fig. 7, patients with 78 and 66 seeds had prostatic calcifications. On CT, calcifications appear with positive contrast-like seeds; however, given the diamagnetic properties (average magnetic susceptibility of -14 ppm) of calcium carbonate, calcifications are depicted with negative contrast on QSM which makes them easily differentiable from positive contrast paramagnetic seeds.

MR-based seed localization and dosimetric analysis

The seed localization algorithm identified all 168 seeds with good spatial accuracy and there was no significant difference between MR- and CT-based seed positions ($p > 0.8$). Figure 8a compares the detected seed centroids using the proposed MR-only and the standard CT-based approaches in the patient with 66 seeds; the MRI- and CT-derived DVH curves for the same patient are shown in Fig. 8b. The comparison between the dosimetric indices in patients is presented in Table 1. The maximum and average distance between MR- and CT-derived seed positions were 2.6 mm and 1.2 ± 0.9 mm, respectively, by applying the proposed algorithm.

The differences in MR- and CT-derived seed positions in each patient approximated to a Gaussian distribution which

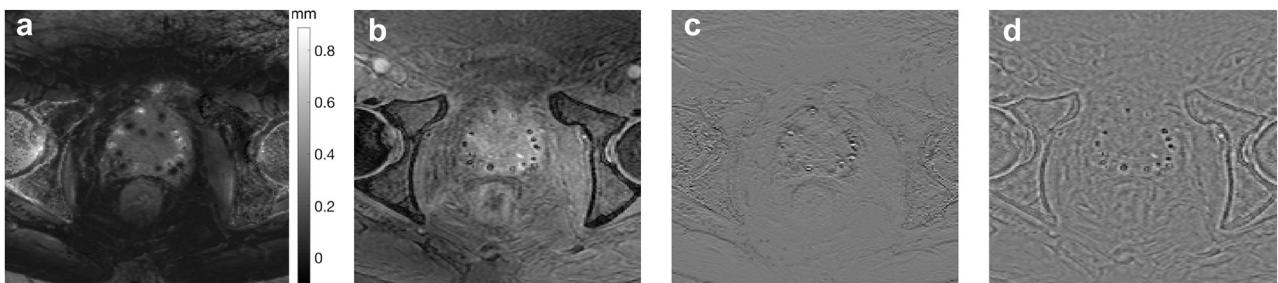


Fig. 4. (a) The estimated distortion map; (b) distortion-corrected magnitude image; (c) difference between corrected and uncorrected magnitude images; (d) corrected magnitude image after edge enhancement.

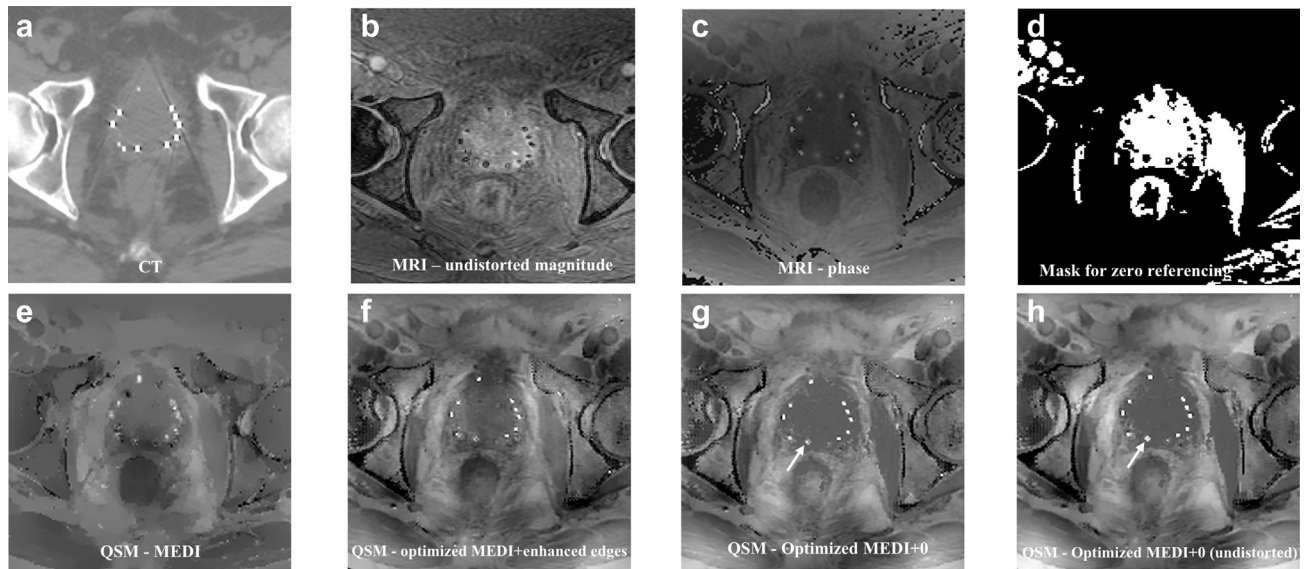


Fig. 5. For one axial slice of the prostate: (a) CT image; (b) MR magnitude image acquired at TE = 2.3 ms; (c) MR phase image acquired at TE = 2.3 ms; (d) estimated prostate and muscle mask for zero referencing during dipole inversion process; (e) the estimated susceptibility map by applying the exact method proposed in the study by Nosrati *et al* (20); (f) the estimated susceptibility map using the proposed workflow with edge enhancement but without distortion correction and prostate zero referencing; (g) the estimated susceptibility map using the proposed workflow with MEDI+0 but without distortion correction; (h) the estimated susceptibility map using the proposed workflow with edge enhancement, MEDI+0 and distortion correction.

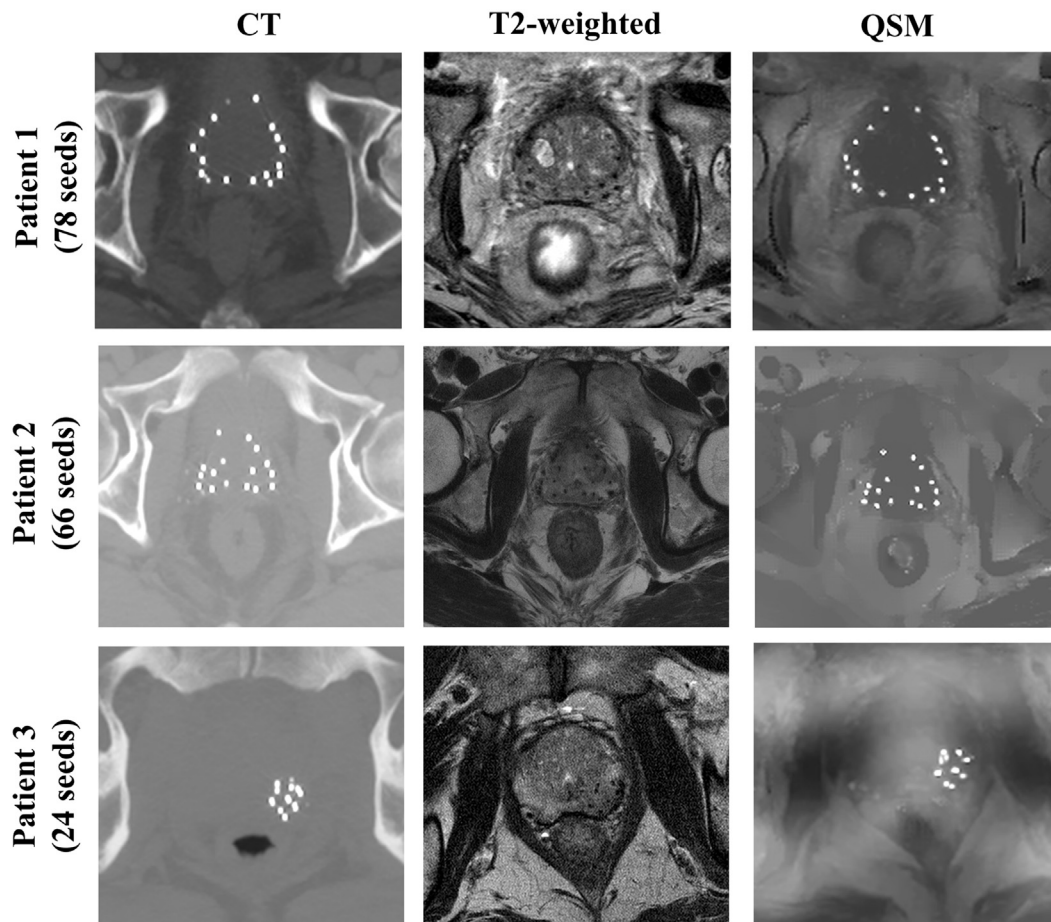


Fig. 6. T2-weighted MR and the MIP reconstruction of five mid-slices (7.5 mm thickness) of CT and QSM of three patients. MIP = maximum intensity projection; QSM = quantitative susceptibility mapping.

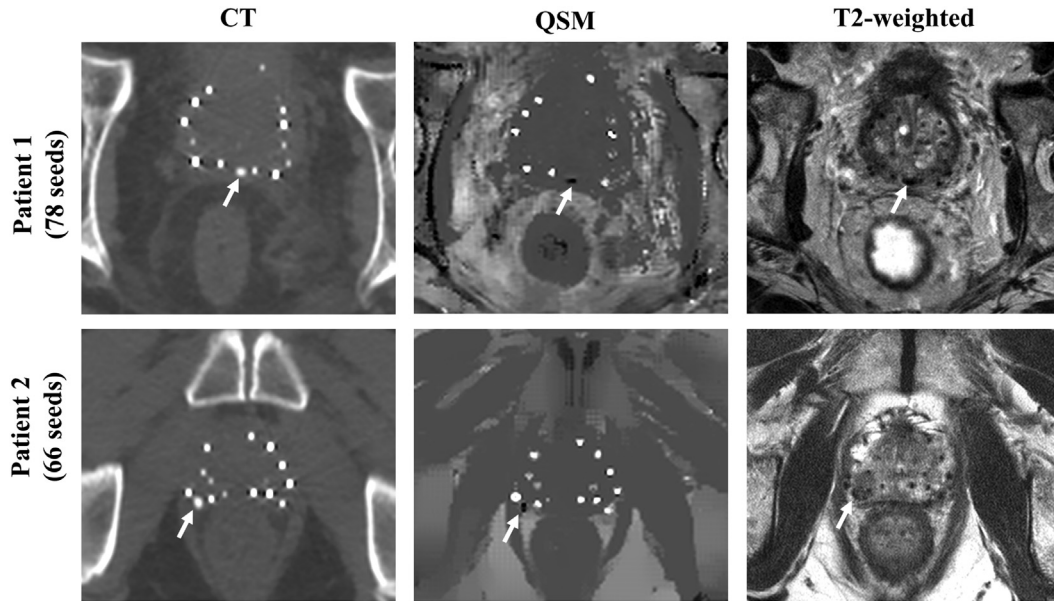


Fig. 7. CT, QSM, and T2-weighted MR images of an axial slice of the prostate which contained a prostatic calcification. The arrows indicate the location of the calcification. QSM = quantitative susceptibility mapping.

was confirmed by Kolmogorov-Smirnov normality test ($p > 0.1$). Bland-Altman analysis of MR-based compared with CT-derived seed centroids revealed a small bias of -0.41 mm with narrow $[-1.85 + 1.04]$ mm 95% limits of agreement. As shown in Fig. 8c, only four of 168 seeds were out of the 95% confidence interval level.

Discussion and conclusion

In comparison with CT, MR imaging provides improved definition of prostate base and apex, and determination of the prostate rectal interface, where, for example, Mashouf et al. (39) have found that at a modest contouring

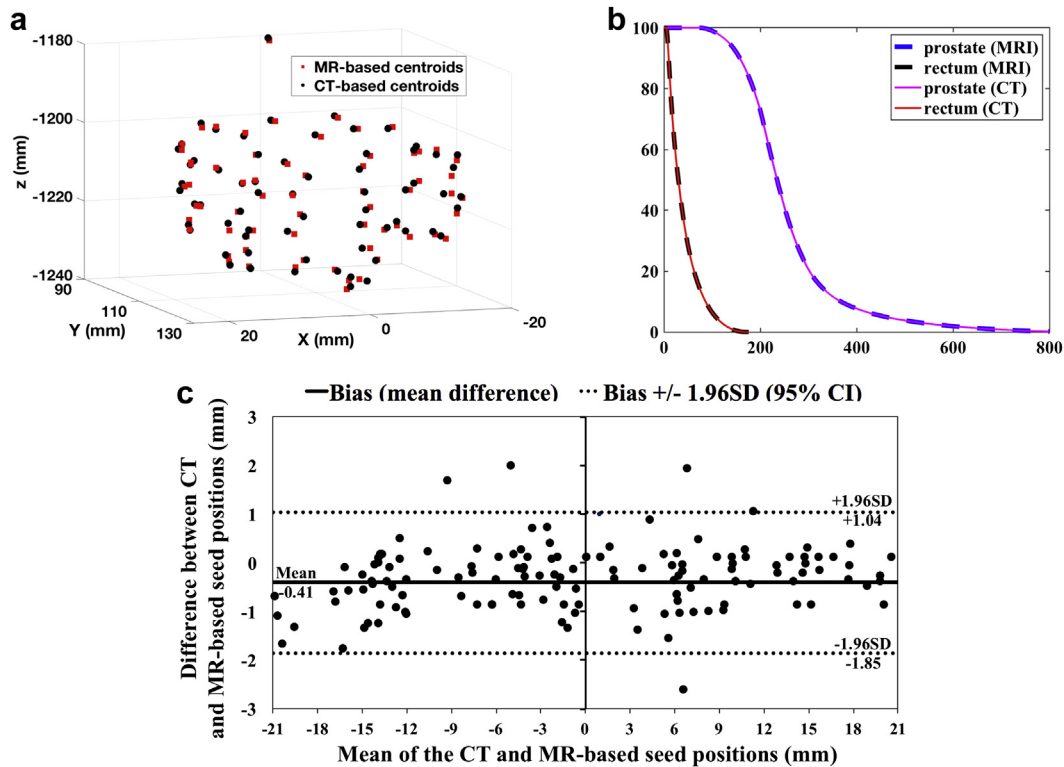


Fig. 8. (a) Comparison between the proposed MR- and CT-derived positions in the patient with 66 implanted seeds; (b) the estimated DVH curves based on CT/MR-derived seed positions for the patient with 66 seeds; (c) Bland-Altman plots of MR-derived vs. CT-derived seed centroids in all three patients. DVH = dose volume histogram.

uncertainty of 2 mm expanded from the original prostate contours decreased the D_{90} by 14.9%. An ideal and powerful approach would be to identify the seeds directly using the MR images thus enabling a true MR-only postimplant plan quality assessment workflow.

Recently Nosrati *et al.* (20) have proposed an MRI-only pipeline for brachytherapy seed visualization and localization which was only validated on simple agar phantoms with small numbers of seeds. The performance of that algorithm was significantly degraded in patients therefore the transition of the technique to the clinic required extensive modifications of the MRI acquisition parameters and postprocessing algorithm. In summary, in the present study, an optimal MRI pulse sequence was proposed, the seed-induced geometrical distortions and intensity artifacts were estimated and corrected; edge enhancement was performed on undistorted magnitude images to improve the morphology-enabled dipole inversion process (40–43), susceptibility mapping workflow was optimized and morphology-enabled dipole inversion with prostate tissue zero referencing (MEDI+0) technique was used, and seed finder algorithm was modified to minimize the localization error in patients. The optimized MRI-only clinical workflow map for postimplant dosimetry of prostate LDR brachytherapy is illustrated in Fig. 9. In this work, CT was only used to validate the MR-based results; however, the proposed workflow is MRI-only.

In general, the susceptibility-induced field distortion depends on the direction of the susceptibility source (which in case of brachytherapy seeds is a long cylinder) and the maximum field distortion occurs when the seeds are transverse to the static field while minimum disturbance is when seeds are parallel to the main field (44); thus theoretically, seed visualization and shape reconstruction through QSM is affected by seed orientation. Although susceptibility-induced phase shift depends on orientation, magnitude

images are minimally affected by seed orientation and in this study, we showed that using morphological information from magnitude images (MEDI) helps to reconstruct the seed shape regardless of their orientation which is critical for accurate seed detection.

The patient-induced field inhomogeneities and the resulting image distortions are of main concern in any MRI-based radiation therapy. In radiation treatment planning, few millimeters of distortion may result in significant error in target delineation and dose calculations; hence, geometrical distortions need to be corrected before MRI-based treatment planning. Recently, it has been shown that, patient-induced distortions could be significantly larger than those from the system (gradient nonlinearity and inhomogeneous B_0) in prostate patients with cancer (40). In this study, the pixel bandwidth was relatively high which potentially minimized the image distortion; however, owing to the presence of high susceptibility implanted seeds, an average distortion of 1.1 mm was observed around the seeds. The image distortion correction before QSM improved the spatial accuracy of seed visualization and localization. Distortion correction could also affect prostate contouring due to susceptibility mismatch between prostate and gas-filled rectum, presence of the seeds at the prostate border, thus joint evaluation of distortion correction on both seed localization and contouring on a large cohort of prostate brachytherapy patients is a potential extension of the present study.

Our results suggest that MEDI+0 significantly improves the homogeneity of the background prostate tissue and reduces artifacts and hypointense shadows at the seed boundaries which are mainly due to the large susceptibility mismatch between seeds and the prostate. The L2-regularization of the prostate susceptibility is similar to the L1-regularization term of the gradients and is considered as an additional prior structural constraint that reduces artifacts around the seeds. Although DBSCAN algorithm

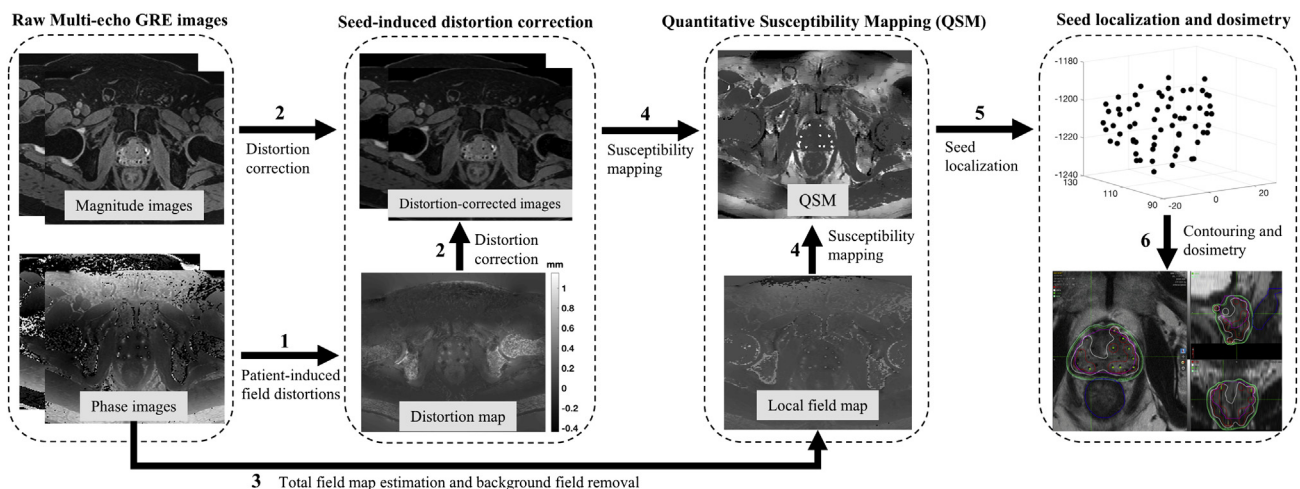


Fig. 9. Schematics of the proposed MRI-only workflow for clinical implementation.

for seed localization handles noise to some extent, enforcing the background (prostate) uniformity improved seed localization accuracy.

This study also showed that the unlike some previous works investigating the feasibility of contrast-enhanced T1-weighted images for MRI-based seed identification (45,46), the performance of the proposed workflow is similar for both intraprostatic and extraprostatic seeds.

The Bland-Altman analysis showed excellent agreement between CT and MRI seed positions in both phantoms and patients. The minor observed differences in seed positions between CT and MRI in patients could be due to the differences in patient positioning and internal prostate motion between the two scans and may not be the error of the proposed workflow. The small differences in seed positions between CT and MRI did not result in any difference in dosimetric parameters which is in agreement with a previous work showing the low sensitivity of prostate dosimetric parameters to seed localization accuracy (47).

In addition to positive contrast seed visualization using QSM, we showed that the proposed method also visualizes prostatic calcifications with negative contrast without any interference. The difference in MR and CT based dose to prostate was less than 2%. It should be noted that the minor observed differences in dosimetric parameters might have been due to the differences in rectal and prostate positions between two scans.

One limitation in application of this technique in the clinic is the extended MR scan time by about 10 min which makes the sequence susceptible to motion artifact. Although the increased scan time may be justified by improved target delineation and overall accuracy, the scan time could be further reduced by optimizing sequence parameters (specially number of signal averages); however, considering the size of the seeds, the resolution must be kept as high as possible. Another limitation of the present work is the small sample size of patients which needs to be addressed by extending the study to a sufficiently larger cohort of patients (e.g., ≥ 20). The exercise of optimizing the imaging and postprocessing sequences of a wide-ranging heterogeneous makeup of tissues in a large cohort will certainly improve the robustness of our approach, where the heterogeneous makeup of tissues may present cases of unique signal distortions/losses in the implanted volume. Finally, to assess the accuracy of the MR-based seed localization, rigid registration was performed between CT- and MR-based seed centroids. Although applying a rigid registration between seed centroids derived from the two modalities avoided the potential CT–MR image fusion error or bias, it may have masked some systematic errors. The systematic errors of the proposed MRI-based seed visualization and identification algorithm may be investigated through quantitative analysis of CT–QSM image fusion by positive contrast seed alignment.

The dosimetric comparisons between CT-only, CT + MRI and MR-only approaches in future work will

provide a further, valuable insight into the overall importance of the MR-only workflow.

In conclusion, this work provided strong evidence that the proposed MRI-only workflow is feasible and possesses a high potential for translation to any clinic.

Acknowledgments

The authors would like to thank IsoAid for providing brachytherapy seeds for phantom studies. R.N. is funded by the NSERC CGS-D3 (grant ID: 489777 - 2016) doctoral scholarship and the study was funded by the Prostate Cancer Canada (grant ID: D2017-1813).

References

- [1] Davis BJ, Horwitz EM, Lee WR, et al. American Brachytherapy Society consensus guidelines for transrectal ultrasound-guided permanent prostate brachytherapy. *Brachytherapy* 2012;11:6–19.
- [2] Ash D, Flynn A, Battermann J, et al. ESTRO/EAU/EORTC recommendations on permanent seed implantation for localized prostate cancer. *Radiother Oncol* 2000;57:315–321.
- [3] Lee WR, Roach M, Michalski J, et al. Interobserver variability leads to significant differences in quantifiers of prostate implant adequacy. *Int J Radiat Oncol Biol Phys* 2002;54:457–461.
- [4] Dubois DF, Prestidge BR, Hotchkiss LA, et al. Intraobserver and interobserver variability of MR imaging- and CT-derived prostate volumes after transperineal interstitial permanent prostate brachytherapy. *Radiology* 1998;207:785–789.
- [5] De Brabandere M, Al-Qaisieh B, De Wever L, et al. CT- and MRI-based seed localization in postimplant evaluation after prostate brachytherapy. *Brachytherapy* 2013;12:580–588.
- [6] Kunogi H, Hojo H, Wakumoto Y, et al. A new two-step accurate CT-MRI fusion technique for post-implant prostate cancer. *J Contemp Brachytherapy* 2015;7:117–121.
- [7] Polo A, Cattani F, Vavassori A, et al. MR and CT image fusion for postimplant analysis in permanent prostate seed implants. *Int J Radiat Oncol* 2004;60:1572–1579.
- [8] Dehghan E, Le Y, Lee J, et al. CT and MRI fusion for postimplant prostate brachytherapy evaluation. *Proc IEEE Int Symp Biomed Imaging* 2016;2016:625–628.
- [9] Zijlstra F, Moerland MA, van der Voort van Zyp JRN, et al. Challenges in MR-only seed localization for postimplant dosimetry in permanent prostate brachytherapy. *Med Phys* 2017;44:5051–5060.
- [10] Kuo N, Lee J, Tempany C, et al. MRI-based prostate brachytherapy seed localization. *Proc IEEE Int Symp Biomed Imaging* 2010;2010:1397–1400.
- [11] Stuber M, Gilson WD, Schär M, et al. Positive contrast visualization of iron oxide-labeled stem cells using inversion-recovery with ON-resonant water suppression (IRON). *Magn Reson Med* 2007;58:1072–1077.
- [12] de Leeuw H, Seevinck PR, Bakker CJG. Center-out radial sampling with off-resonant reconstruction for efficient and accurate localization of punctate and elongated paramagnetic structures. *Magn Reson Med* 2013;69:1611–1622.
- [13] Dong Y, Chang Z, Xie G, et al. Susceptibility-based positive contrast MRI of brachytherapy seeds. *Magn Reson Med* 2015;74:716–726.
- [14] Shi C, Xie G, Zhang Y, et al. Accelerated susceptibility-based positive contrast imaging of MR compatible metallic devices based on modified fast spin echo sequences. *Phys Med Biol* 2017;62:2505–2520.
- [15] Dahnke H, Liu W, Herzka D, et al. Susceptibility gradient mapping (SGM): A new postprocessing method for positive contrast generation applied to superparamagnetic iron oxide particle (SPIO)-labeled cells. *Magn Reson Med* 2008;60:595–603.

- [16] Lim TY, Kudchadker RJ, Wang J, et al. Development of a magnetic resonance imaging protocol to visualize encapsulated contrast agent markers in prostate brachytherapy recipients: Initial patient experience. *J Contemp Brachytherapy* 2016;8:235–242.
- [17] Lim TY, Stafford RJ, Kudchadker RJ, et al. MRI characterization of cobalt dichloride-N-acetyl cysteine (C4) contrast agent marker for prostate brachytherapy. *Phys Med Biol* 2014;59:2505–2516.
- [18] Frank SJ, Stafford RJ, Bankson JA, et al. A novel MRI marker for prostate brachytherapy. *Int J Radiat Oncol Biol Phys* 2008;71:5–8.
- [19] Martin GV, Ma J, Kudchadker RJ, et al. Automated prostate brachytherapy seed detection on post-implant MRI using novel martin algorithm. *Brachytherapy* 2017;16:S57.
- [20] Nosrati R, Soliman A, Safigholi H, et al. MRI-based automated detection of implanted low dose rate (LDR) brachytherapy seeds using quantitative susceptibility mapping (QSM) and unsupervised machine learning (ML). *Radiother Oncol* 2018;129:540–547.
- [21] Fessler JA. Michigan image reconstruction toolbox. Available at: <https://web.eecs.umich.edu/~fessler/code/>. Accessed August 10, 2018.
- [22] Fessler JA. Conjugate-gradient preconditioning methods: Numerical results. *communications & signal processing laboratory of The University of Michigan Ann Arbor, Michigan, Technical Report No. 303* January 1997. Available at: <https://pdfs.semanticscholar.org/11e1/3bc752ffdaac28a11340126f22635660666c.pdf>.
- [23] Matakos A, Balter J, Cao Y. Estimation of geometrically undistorted B_0 inhomogeneity maps. *Phys Med Biol* 2014;59:4945–4959.
- [24] Fessler JA, Rogers WL. Spatial resolution properties of penalized-likelihood image reconstruction: Space-invariant tomographs. *IEEE Trans Image Process* 1996;5:1346–1358.
- [25] Matakos A, Fessler JA. Joint estimation of image and fieldmap in parallel MRI using single-shot acquisitions. In: *2010 IEEE International Symposium on Biomedical Imaging: From Nano to Macro*. IEEE; 2010. p. 984–987.
- [26] de Rochefort L, Brown R, Prince MR, et al. Quantitative MR susceptibility mapping using piece-wise constant regularized inversion of the magnetic field. *Magn Reson Med* 2008;60:1003–1009.
- [27] Jackson JD. *Classical electrodynamics*. NJ: John Wiley and Sons; 1999.
- [28] Liu T, Khalidov I, De Rochefort L, et al. A novel background field removal method for MRI using projection onto dipole fields (PDF). *NMR Biomed* 2011;24:1129–1136.
- [29] Liu J, Liu T, de Rochefort L, et al. Morphology enabled dipole inversion for quantitative susceptibility mapping using structural consistency between the magnitude image and the susceptibility map. *Neuroimage* 2012;59:2560–2568.
- [30] Liu Z, Spincemaille P, Yao Y, et al. MEDI+0: Morphology enabled dipole inversion with automatic uniform cerebrospinal fluid zero reference for quantitative susceptibility mapping. *Magn Reson Med* 2018;79:2795–2803.
- [31] Liu T, Wisnieff C, Lou M, et al. Nonlinear formulation of the magnetic field to source relationship for robust quantitative susceptibility mapping. *Magn Reson Med* 2013;69:467–476.
- [32] Liu T, Liu J, de Rochefort L, et al. Morphology enabled dipole inversion (MEDI) from a single-angle acquisition: Comparison with COSMOS in human brain imaging. *Magn Reson Med* 2011;66:777–783.
- [33] Wang Y, Liu T. Quantitative susceptibility mapping (QSM): Decoding MRI data for a tissue magnetic biomarker. *Magn Reson Med* 2015;73:82–101.
- [34] Kroon D-J, Slump CH. Coherence filtering to enhance the mandibular canal in cone-beam CT data. In: *Proceedings of the 4th Annual Symposium of the IEEE-EMBS Benelux Chapter*. IEEE EMBS Benelux Chapter; 2009. p. 41–44.
- [35] Sander J, Ester M, Kriegel H-P, et al. Density-based clustering in spatial databases: The algorithm GDBSCAN and its applications. *Data Min Knowl Discov* 1998;2:169–194.
- [36] Park H-S, Jun C-H. A simple and fast algorithm for K-medoids clustering. *Expert Syst Appl* 2009;36:3336–3341.
- [37] Ester M, Kriegel H-P, Sander J, et al. A density-based algorithm for discovering clusters a density-based algorithm for discovering clusters in large spatial databases with noise. *Proc Second Int Conf Knowl Discov Data Min* 1996;226–231.
- [38] Besl PJ, McKay ND. A method for registration of 3-D shapes. *IEEE Trans Pattern Anal Mach Intell* 1992;14:239–256.
- [39] Mashouf S, Safigholi H, Merino T, et al. Sensitivity of clinically relevant dosimetric parameters to contouring uncertainty in postimplant dosimetry of low-dose-rate prostate permanent seed brachytherapy. *Brachytherapy* 2016;15:774–779.
- [40] Adjeiwaah M, Bylund M, Lundman JA, et al. Quantifying the effect of 3T magnetic resonance imaging residual system distortions and patient-induced susceptibility distortions on radiation therapy treatment planning for prostate cancer. *Int J Radiat Oncol* 2018;100:317–324.
- [41] Lee YK, Bollet M, Charles-Edwards G, et al. Radiotherapy treatment planning of prostate cancer using magnetic resonance imaging alone. *Radiother Oncol* 2003;66:203–216.
- [42] Khoo VS, Dearnaley DP, Finnigan DJ, et al. Magnetic resonance imaging (MRI): Considerations and applications in radiotherapy treatment planning. *Radiother Oncol* 1997;42:1–15.
- [43] Wang H, Balter J, Cao Y. Patient-induced susceptibility effect on geometric distortion of clinical brain MRI for radiation treatment planning on a 3T scanner. *Phys Med Biol* 2013;58:465–477.
- [44] Schenck JF. The role of magnetic susceptibility in magnetic resonance imaging: MRI magnetic compatibility of the first and second kinds. *Med Phys* 1996;23:815–850.
- [45] Buch K, Morancy T, Kaplan I, et al. Improved dosimetry in prostate brachytherapy using high resolution contrast enhanced magnetic resonance imaging: A feasibility study. *J Contemp Brachytherapy* 2014;4:337–343.
- [46] Ohashi T, Momma T, Yamashita S, et al. Impact of MRI-based post-implant dosimetric assessment in prostate brachytherapy using contrast-enhanced T1-weighted images. *Brachytherapy* 2012;11:468–475.
- [47] Su Y, Davis BJ, Furutani KM, et al. Dosimetry accuracy as a function of seed localization uncertainty in permanent prostate brachytherapy: Increased seed number correlates with less variability in prostate dosimetry. *Phys Med Biol* 2007;52:3105–3119.